Gravity Effect on Thermal-solutal Convection during Solidification Revealed by Four-dimensional Synchrotron Imaging with Compositional Mapping

T. Nelson [a], B. Cai [a,*], N. Warnken [a], P.D. Lee [b], E. Boller [c], Oxana Magdysyuk [d], Nick Green [a]

[a] School of Metallurgy and Materials, University of Birmingham, B15 2TT UK
[b] Mechanical Engineering, University College London, WC1E 7JE, UK
[c] Diamond Light Source Ltd, Harwell Science and Innovation Campus, Didcot, OX11 0DE, UK
[d] ESRF-The European Synchrotron, 71 Avenue des Martyrs, 38000 Grenoble, France

Corresponding author: B.C. b.cai@bham.ac.uk

Abstract

The effect of gravity on thermo-solutal convection and its impact on solidification dynamics of an Al-15wt%Cu alloy were studied using high speed synchrotron tomography. A method for mapping the composition of the solidifying sample was developed, enabling three-dimensional quantification of the time evolved solute concentration and dendrite morphology. Differences in solute segregation, dendrite morphology and fragmentation between upwards and downwards solidification were identified, which were attributed to buoyancy-modulated thermal-solutal convection.

Keywords: Solidification, Gravity, 4D, Synchrotron tomography

Gravity plays an inherent role during liquid metal processing on Earth based conditions, affecting the microstructures and properties of cast components. Additionally, manufacturing of metals and alloys in Space and on other planets is under consideration and development [1], during which different gravity conditions are experienced. Therefore, it is of great importance to illustrate the impact of gravity on solidification. Besides, insights into this can help understand the crystallization of many other systems, from bio-crystals to magmas.

Gravity can modulate the convective flow during solidification as a result of the interaction between buoyancy-induced and thermal-solutal flow, leading to the change of constitutional undercooling [2–4], solute distribution [5–8], and crystal floatation [7,9]. These effects can cause a multitude of microstructural changes during solidification, including interface instability [8,10–12], solute segregation [8,13], columnar to equiaxed transition [2,14–17] and dendrite array spacing [18–20]. The disrupting effects of gravity have been studied numerically and experimentally. Microstructual simulations have demonstrated that buoyancy has a significant effect on the spacing of dendritic arrays and solute segregation [21]. Experimentally, *in situ* and real-time observation has been a method of choice to enlighten gravity effects on solidification, which includes optical microscopy using transparent organic alloys [17] and 2D X-ray radiographs [2,15,22,23] of metallic alloys. Experiments have been carried out on Earth [5], aboard the International Space Station [2,23], parabolic flights [9], and sounding rockets (for example the MASER-12 mission in 2012 [24]). These studies have greatly enhanced our understanding of the gravity effects. Most of these studies use analogue samples which may not truly represent metallic materials, while thin metallic materials for radiographic observation might not provide us with the bulk 3D information. High speed synchrotron tomography allows 4D (3D plus time) observation of relatively bulky metallic samples, used extensively to study

alloy solidification [25–27]. With the x-ray tomographic technique, 3D topological transition can be qualified with ease, but 3D mapping of solute elements during solidification has not been reported.
Here, *in situ* observation of the upwards and downwards directional solidification of Al-15wt.%Cu was performed using the temperature gradient stage [27], imaged by high speed synchrotron tomography. A methodology was developed to construct the 3D solute distribution during solidification enabling 4D (3D space + time) imaging together with composition information. This allows us to compare the solute segregation behaviour and dendrite morphology of solidifying alloys under different gravity conditions. The work provides benchmark cases for numerical simulation of solidification considering the effect of gravity, paving the way for the prediction of solidification dynamics in other gravitational conditions.

Fig. 1a shows a schematic of the experimental set-up, including the temperature gradient furnace, and the high-speed tomography system at ID19, Europe Synchrotron Radiation Facility. The experimental conditions for the tomographic imaging can be found in Ref. [27]. Tomograms were recorded in 1 s with 1000 projects over 180°. The sample was rotated at 2 s per rotation for tomographic data collection. There were 15 s waiting time between two consecutive tomograms for data downloading. The voxel size of the tomography is 2.2 μm. Upwards and downwards directional solidification were carried out on Al15wt%Cu samples using the power down method [27] (Fig. 1b). The samples were first melted using the temperature gradient stage with a temperature gradient established between the hot and cold heaters. The two heaters then cool down at the same rate, maintaining the temperature gradient. For upwards solidification, a temperature gradient of 10 K/mm and cooling rate of 0.05 K/s were used, whereas the downwards solidification was performed under a temperature gradient of 12 K/mm and cooling rate of 0.05 K/s. The temperatures were measured by thermocouples slightly away from the sample hence the sample temperature might be slightly different from the measured temperatures by the thermocouples.

The reconstructed tomographic data was analysed by Avizo 9.4 (ThermoFisher Scientific) and ImageJ (US NIH, Bethesda, MD, USA) with procedures detailed in [27]. Anisotropic diffusion was used for noise reduction and Otsu-based threshold was used to segment the primary phase from the liquid. We applied the Cu concentration mapping on the datasets after noise reduction. The Cu concentration mapping was made possible because the grey value of the X-ray images at each voxel is a linear function of density (absorption coefficient) of the material at that voxel. We also assumed that at the liquid state before solidification (Fig. 1d), the Cu concentration of liquid Al-15Cu is 15 wt%. At the end of solidification (Fig. 1e), the Cu concentration in the residual liquid increases to the eutectic composition of 33 wt% due to segregation, whereas the Cu concentration in the solid phase is 5.7 wt% according to the Al-Cu phase diagram. The darker dendritic structure in Fig.1e are the primary phase. By measuring the grey values of the recorded tomographic images (16 bit unsigned) for the three afore-mentioned conditions, a linear relationship between Cu concentration and grey values of the tomograms can be derived. Equations (Fig. 1c) were found for upwards and downwards solidification, respectively, and were used to map Cu concentration for all the tomographic data. The two equations are fairly similar while the small difference is due to the change in X-ray flux between the two experiments. Similar procedures were applied to in situ radiographic imaging of solidification [28–30]. In the future, to further validate the equations, it is suggested to carry out a tomographic scan of the post-mortem specimen and compare it with composition mapping using EDS.

Fig. 2a-d show four vertical slices from the central plane of the Al-15wt%Cu sample solidifying upwards over four-time steps (t = 76, 166, 346 and 796 s) whereas Fig. 2f-i shows the sample solidifying downwards (at t = 76, 166, 346 and 796 s). Supplementary Videos 1 and 2 show the upwards and downwards solidification, respectively. The primary dendrite phase is blue, while copper enriched liquid is green/red. By observation, a qualitative understanding of the segregation behaviour can be revealed. In Fig. 2a-d, as the dendritic structure initially develops from the bottom of the field-of-view (FOV), copper begins to accumulate at the lower right portion of the FOV (circled). A macro-segregation zone is formed there, which is confirmed by a central transverse slice (Fig. 2e). The explanation for this phenomenon relies on the relative difference in liquid density resulting from varying copper content. Hence, the increased density of Cu-enriched liquid causes flow towards the depressed region resulting in visible copper accumulation (Fig. 2c).

Fig. 2f-i show the central planes from a sample solidified downwards. In contrast to upwards solidification, Cu-enriched liquid is observed in the interdendritic region, as confirmed in a central transverse slice (Fig. 2j) and no radial macro-segregation was observed. Solute plumes have been reported [9] via in situ radiography during downwards solidification, but it is not observed here. During downwards solidification, it is likely that some of the segregated solute is immediately transported into the hot liquid below the growth front and is mixed due to a convection current established in this region. Whereas the remainder of the copper is rejected into the semi permeable interdendritic region [31] and is unable to flow downwards causing accumulation in this region. 2D simulations have shown a similar phenomenon, in which plumes of solute rich liquid are ejected below the growth front but Cu accumulation occurs between the dendrites [21]. The results clearly show the difference between thin radiographic samples and our more realistic 3D results.

Fig. 3a-d and Fig. 3e-f show 3D renderings, after segmentation, of the solid phase during upwards and downwards solidification respectively, allowing further examination of the microstructural development. The full sequences are shown in Supplementary **Videos 3 and 4**. Again by observation, a comparative evaluation of the differing gravity conditions with respect to growth direction can be explored.

During upwards solidification (Fig. 3a-d), a tilted solid-liquid interface was observed. The development of this feature may initially be due to the transverse/radial temperature gradient arising from the different thermal conductivity of the sample and the outer crucible, as was suggested by Nguyen-Thi et al [13]. This develops into a large region, free of solid phase at the early stage of solidification which developed into a macro-segregation zone. As solute accumulates in this region, solidification is retarded and hence dendrites are only able to form at the later stage of the solidification. Only two large dendrite trunks evolve in the sample, with well-developed secondary and tertiary arms observed. Similar dendrite clustering phenomena have been observed using x-ray radiography [6,13]. Whereas for downwards solidification (Fig. 3e-f), dendrites are smaller with less developed side branches. The distortion of the growth front is also reduced, showing an almost flat and levelled interface between liquid and the mushy zone.

Quantification of the morphological differences due to gravity effects can be obtained using the equation below [20] to calculate primary dendrite arm spacing (λ):

$$\lambda = c\sqrt{\frac{A}{n}}$$ Eq.1.

Where c = coefficient depending on dendritic structure (0.5 for random), A = cross sectional area of sample and n = number of dendrites. The primary arm spacing (λ), was estimated to be $\lambda_{upwards}$=564 μm, and $\lambda_{downwards}$=178 μm for upwards solidification and downwards solidification, respectively. This supports the visual observations that primary dendrite arms are much larger during upwards solidification than downwards solidification.

Steinbach [21] proposed a scaling law derived from a phase field simulation which calculated the primary dendrite arm spacing for different levels of gravity [21]. Values of primary arm spacing can also be determined to be $\lambda_{upwards}'$ =514μm, and $\lambda_{downwards}'$=176 μm for upwards and downwards solidification on Earth according to the scaling low, which agree well with our experimental measurements according to Eq.1. ($\lambda_{upwards}$=564μm, and $\lambda_{downwards}$ =178μm). Steinbach suggested [21], during upwards solidification, segregated heavy Cu solute flows downwards and is transported to the interdendritic region, leading to the accumulation of solute there and an increase of the dendrite spacing. During downwards solidification, segregated copper immediately descends, transported out of the interdendritic regions, leading to solute depletion at the growth interface and increasing the interfacial undercooling across the whole sample area, leading to a decrease in dendrite spacing. At the later stage, copper accumulates in the interdendritic region due to the decrease of permeability [21].

Dendrite fragmentation is observed in Fig. 3a-d for upwards solidification (highlighted by circles in Fig. 3a and 3b). Small fragments, visible in Fig. 3a and 3b (circled in red), can be seen to float up and then re-melt in the hotter liquid, as also observed in the literature [6,7,9]. One fragment develops into a large equiaxed dendrite (green circle in Fig. 3a and Supplementary Video 5). This is because after it detaches from the main trunk, it is transported upwards and subsequently attaches to a pore, avoiding floating to the hot region and being melted. Conversely, there are no fragments visible during downwards solidification (Fig. 3e-h), as can be seen on Supplementary Video 4.

Dendrite fragmentation has been observed in prior studies using 4D synchrotron tomographic imaging[32], and it was proposed that fragmentation could be attributed to a combined effect of local re-melting and stress concentration. The cross-sectional area of the dendrite root is continuously reduced due to local re-melting by the flow-in hot Cu-enriched liquid. During upwards solidification, a vertical buoyancy force was applied to the dendrite tip as the dendrites are lighter than the surrounding liquid. A stress was also concentrated on this narrow dendrite root, leading to fragmentation from the main structure. However, this is not the case for downwards solidification because the buoyancy direction – the driving force for fracture of the dendrites– is anti-parallel to the dendrite growth direction.

In conclusion, we used 4D (space and time) tomography with additional compositional maps to image upwards and downwards directional solidification of Al-15wt%Cu, relative to gravity. The contrasting microstructures observed, and the underlying mechanisms are summarised in schematic diagrams Fig. 4a and 4b, respectively. During upwards solidification,

macrosegregation and well-developed large dendrite trunks were observed together with fragmentation. However, during downwards solidification, much finer dendrites grew, without dendrite fragmentation nor significant macrosegregation. The difference can be attributed to the buoyancy force that modulated the solute flow convection and that stressed the dendrite arms. Our results show that refined microstructures without macro segregation and fragmentation, all of which are beneficial for mechanical properties, can be obtained if the melt flow direction due to gravity and primary phase growth direction induced by the temperature gradient are the same. The insights we gained from this study will be beneficial to Bridgman casting of Ni-based alloys, fundamental solidification science, and manufacturing in Space. The data we obtained can be used to validate models developed aiming to predict the microstructure of components casted under varying gravity conditions.

References:

[1] M.Z. Naser, Acta Astronaut. 155 (2019) 264–273.
[2] Y.Z. Li, N. Mangelinck-Noël, G. Zimmermann, L. Sturz, H. Nguyen-Thi, J. Cryst. Growth 513 (2019) 20–29.
[3] T.S. Prassana Kumar, in: Compr. Mater. Process., Elsevier, 2014, pp. 235–257.
[4] M. Wu, A. Ludwig, Acta Mater. 57 (2009) 5621–5631.
[5] H. Nguyen-Thi, A. Bogno, G. Reinhart, B. Billia, R.H. Mathiesen, G. Zimmermann, Y. Houltz, K. Löth, D. Voss, A. Verga, F. De Pascale, J. Phys. Conf. Ser. 327 (2011).
[6] H. Nguyen-Thi, G. Reinhart, G. Salloum-Abou-Jaoude, D.J. Browne, A.G. Murphy, Y. Houltz, J. Li, D. Voss, A. Verga, R.H. Mathiesen, G. Zimmermann, Microgravity Sci. Technol. 26 (2014) 37–50.
[7] G. Zimmermann, M. Hamacher, L. Sturz, J. Cryst. Growth 512 (2019) 47–60.
[8] A. Bogno, H. Nguyen-Thi, A. Buffet, G. Reinhart, B. Billia, N. Mangelinck-Noël, N. Bergeon, J. Baruchel, T. Schenk, Acta Mater. 59 (2011) 4356–4365.
[9] H. Soltani, G. Reinhart, M.C. Benoudia, M. Zahzouh, H. Nguyen-Thi, IOP Conf. Ser. Mater. Sci. Eng. 529 (2019) 012019.
[10] S. Louhenkilpi, Continuous Casting of Steel, 2014.
[11] P.K. Galenko, V.A. Žuravlev, Physics of Dendrites, World Scientific, 1994.
[12] D.M. Herlach, P.K. Galenko, D. Holland-Moritz, Metastable Solids from Undercooled Melts, 1st Editio, Elsevier, Amsterdam, 2007.
[13] H.N. Thi, Y. Dabo, B. Drevet, M.D. Dupouy, D. Camel, B. Billia, J.D. Hunt, A. Chilton, J. Cryst. Growth 281 (2005) 654–668.
[14] H. Nguyen-Thi, G. Reinhart, N. Mangelinck-Noël, H. Jung, B. Billia, T. Schenk, J. Gastaldi, J. Härtwig, J. Baruchel, Metall. Mater. Trans. A Phys. Metall. Mater. Sci. 38 A (2007) 1458–1464.
[15] L. Abou-Khalil, G. Salloum-Abou-Jaoude, G. Reinhart, C. Pickmann, G. Zimmermann, H. Nguyen-Thi, Acta Mater. 110 (2016) 44–52.
[16] R.H. Mathiesen, L. Arnberg, P. Bleuet, A. Somogyi, Metall. Mater. Trans. A Phys. Metall. Mater. Sci. 37 (2006) 2515–2524.
[17] J.A. Dantzig, M. Rappaz, Solidification, EPFL Press, 2009.
[18] W. Huang, L. Wang, Sci. China Technol. Sci. 55 (2012) 377–386.
[19] C.C. Battalle, R.N. Grugel, A.B. Hmelo, T.G. Wang, Metall. Mater. Trans. A 25 (1994) 865–870.
[20] M.A. Tschopp, J.D. Miller, A.L. Oppedal, K.N. Solanki, Metall. Mater. Trans. A Phys. Metall. Mater. Sci. 45 (2014) 426–437.
[21] I. Steinbach, Acta Mater. 57 (2009) 2640–2645.
[22] R.H. Mathiesen, L. Arnberg, F. Mo, T. Weitkamp, A. Snigirev, Phys. Rev. Lett. 83 (1999) 5062–5065.
[23] Y.Z. Li, N. Mangelinck-Noël, G. Zimmermann, L. Sturz, H. Nguyen-Thi, J. Alloys Compd. 749 (2018) 344–354.
[24] H. Nguyen-Thi, G. Reinhart, G. Salloum Abou Jaoude, R.H. Mathiesen, G. Zimmermann, Y. Houltz, D. Voss, a. Verga, D.J. Browne, a. G. Murphy, J. Cryst. Growth 374 (2013) 23–30.
[25] O. Ludwig, M. Dimichiel, L.U.C. Salvo, M. Suéry, P. Falus, Metall. Mater. Trans. A 36 (2005) 1515–1523.
[26] N. Limodin, L. Salvo, E. Boller, M. Suéry, M. Felberbaum, S. Gailliègue, K. Madi, Acta Mater. 57 (2009) 2300–2310.
[27] B. Cai, A. Kao, P.D. Lee, E. Boller, H. Basevi, A.B. Phillion, A. Leonardis, K. Pericieous, Scr. Mater. 165 (2019) 29–33.
[28] E. Liotti, C. Arteta, A. Zisserman, A. Lui, V. Lempitsky, P.S. Grant, Sci. Adv. 4 (2018) 1–10.
[29] N. Shevchenko, O. Roshchupkina, O. Sokolova, S. Eckert, J. Cryst. Growth 417 (2015) 1–8.

[30] D. Ruvalcaba, R.H. Mathiesen, D.G. Eskin, L. Arnberg, L. Katgerman, Acta Mater. 55 (2007) 4287–4292.
[31] S. Ganesan, C.L. Chan, D.R. Poirier, Mater. Sci. Eng. A 151 (1992) 97–105.
[32] B. Cai, J. Wang, A. Kao, K. Pericleous, A.B. Phillion, R.C. Atwood, P.D. Lee, Acta Mater. 117 (2016) 160–169.

Acknowledgement

This work was supported by the UK-EPSRC (EP/K007734/1) and NERC (NE/M013561/1). The authors thank the European Synchrotron Radiation Facility for providing the beamtime (MA2989) and staff at ID19 beamline for support. B.C. acknowledges the support from the Diamond Birmingham Collaboration and the Alan Turing Fellowship. P.D.L. acknowledges funding from the Royal Academy of Engineering Chair In Emerging Technology.

Figures

Figure 1 (a) Schematic of Furnace; (b) Schematic illustration of upwards and downwards solidification, adapted from Soltani et al [10]; (c) Mean Grey Value plotted against Cu composition. Blue line – Downwards solidification; Red line – Upwards solidification; (d) Fully liquid image of Al 15wt%Cu; (e) Dendritic image at the final stage of solidification where the solid phase is Al 5.5wt%Cu and the liquid Al 33wt%Cu.

Figure 2 (a – e): Upward solidification, (f – j) Downwards solidification.
2D vertical slices, Cu Mapped and Colour Mapped (4 Time steps). (e+j) Transverse slices.

Figure 3 (a-d): 3D Volume render of upwards dendrite growth, (e-h): 3D Volume render of downwards dendrite growth (4 Time steps)

Figure 4 (a) Schematic of dendrite solidifying upwards, with segregated copper settling at the bottom of the sample; (b) Schematic of dendrite solidifying downwards, some segregated copper sits in the interdendritic region and some forms plumes ahead of the interface.

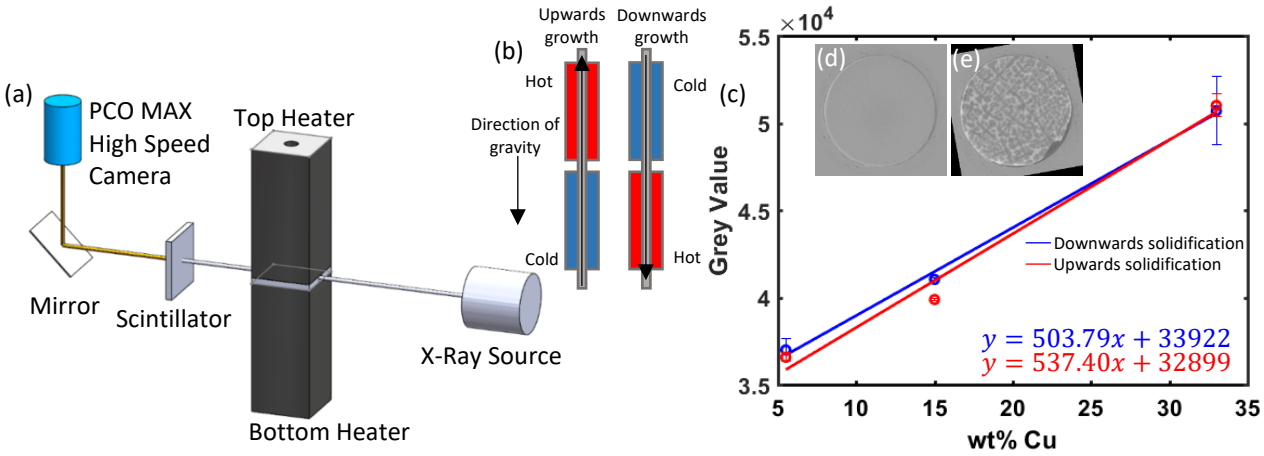

Fig. 1. (a) Schematic of Furnace; (b) Schematic illustration of upwards and downwards solidification, adapted from Soltani et al [10]; (c) Mean Grey Value plotted against Cu composition. Blue line – Downwards solidification; Red line – Upwards solidification; (d) Fully liquid image of Al 15wt%Cu; (e) Dendritic image at the final stage of solidification where the solid phase is Al 5.5wt%Cu and the liquid Al 33wt%Cu.

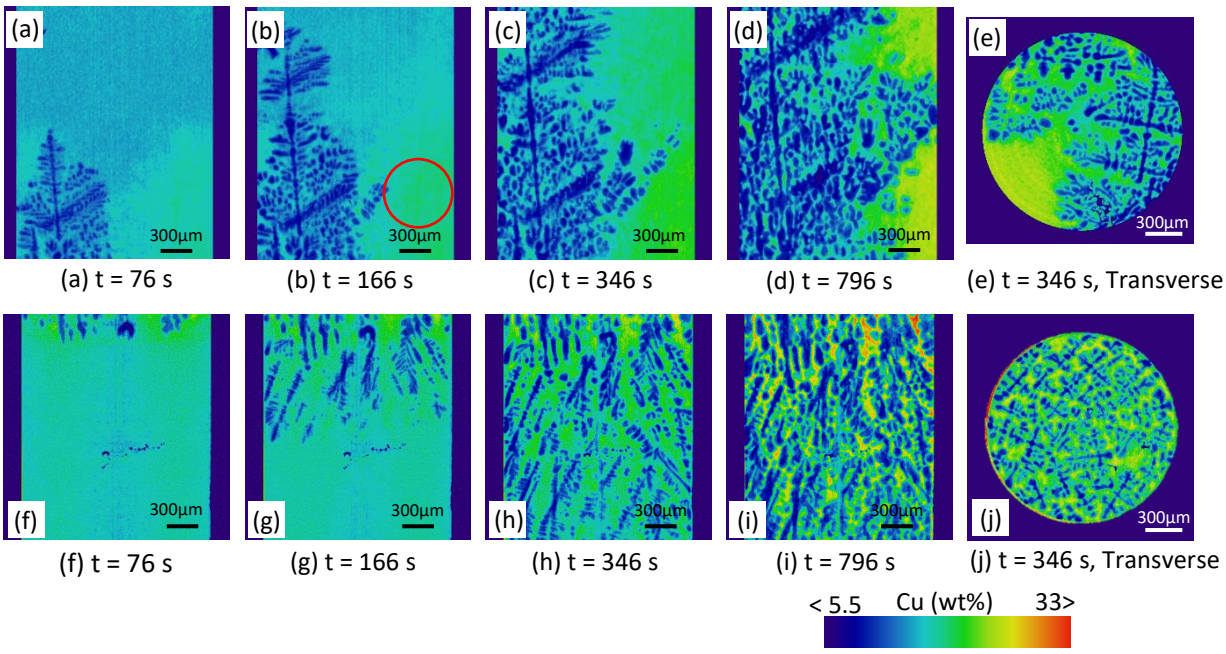

Fig. 2. (a – e): Upward solidification, (f – j) Downwards solidification.
2D vertical slices, Cu Mapped and Colour Mapped (4 Time steps). (e+j) Transverse slices.

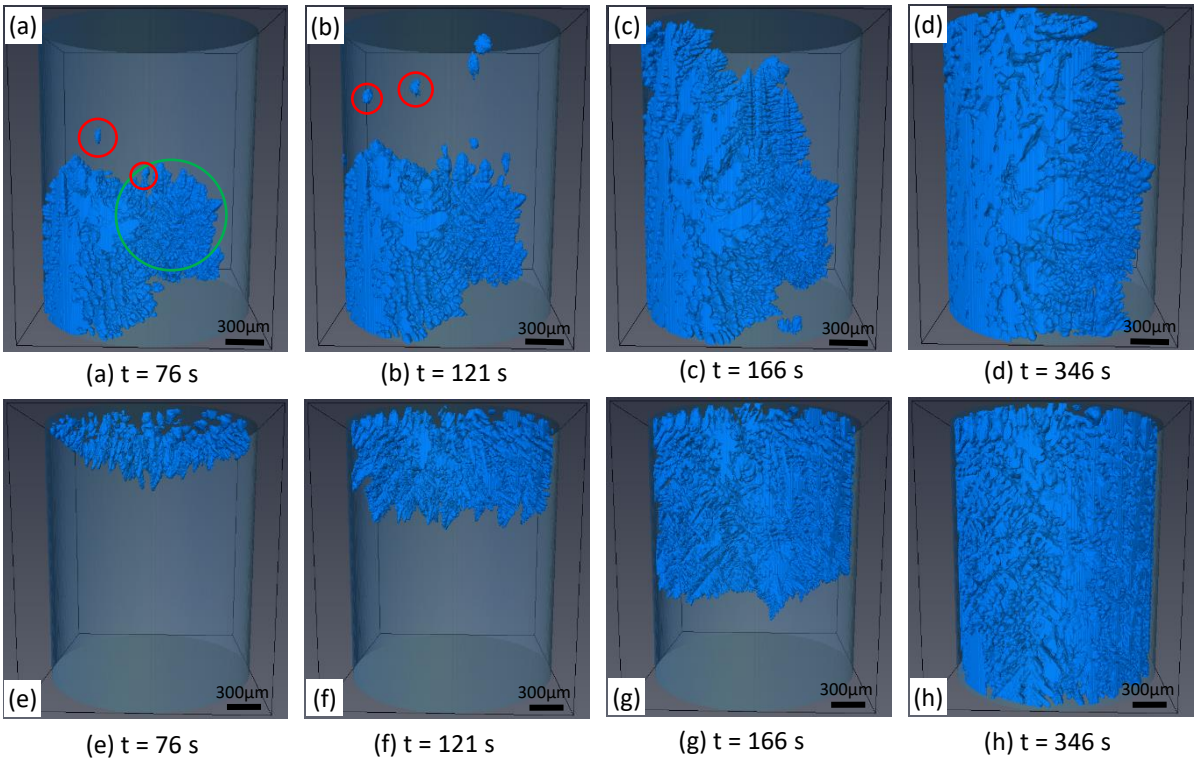

Fig. 3 (a-d): 3D Volume render of upwards dendrite growth, (e-h): 3D Volume render of downwards dendrite growth (4 Time steps)

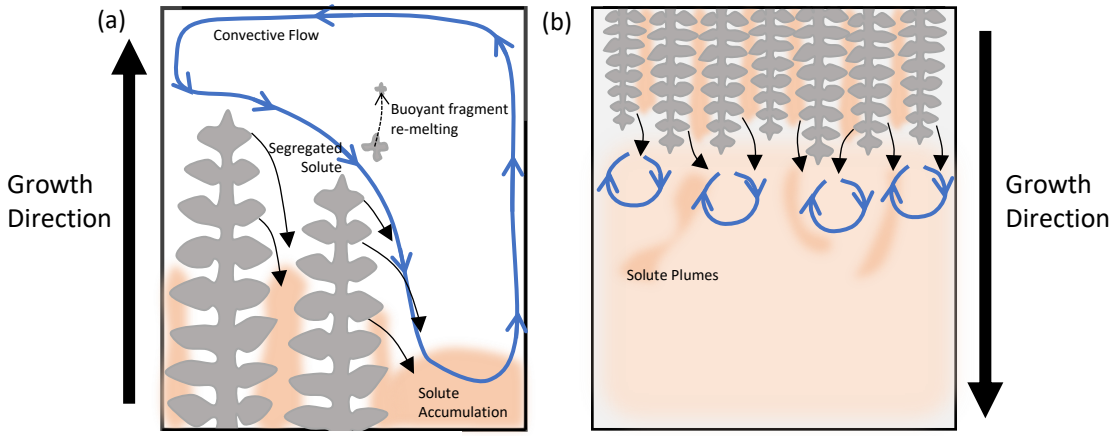

Fig. 4(a) Schematic of dendrite solidifying upwards, with segregated copper settling at the bottom of the sample; (b) Schematic of dendrite solidifying downwards, some segregated copper sits in the interdendritic region and some forms plumes ahead of the interface.